

Article

Effect of the Particle Size of Iron Ore on the Pyrolysis Kinetic Behaviour of Coal-Iron Ore Briquettes

Heng Zheng¹, Wei Wang^{1,*}, Runsheng Xu^{1,2,*}, Rian Zan³, Johannes Schenk² and Zhengliang Xue¹

¹ State Key Laboratory of Refractories and Metallurgy, Wuhan University of Science and Technology, Wuhan 430081, China; zhengheng6728@163.com (H.Z.); xuezhengliang@wust.edu.cn (Z.X.)

² Montanuniversität Leoben, Franz-Josef-Straße 18, A-8700 Leoben, Austria; Johannes.Schenk@unileoben.ac.at

³ Key Laboratory for Ferrous Metallurgy and Resources Utilization of Ministry of Education, Wuhan University of Science and Technology, Wuhan 430081, China; ZanRian163@163.com

* Correspondence: wangwei74@wust.edu.cn (W.W.); xu_runsheng@163.com (R.X.);
Tel.: +86-139-714-365-42 (W.W.); +86-188-104-909-45 (R.X.)

Received: 25 August 2018; Accepted: 25 September 2018; Published: 29 September 2018



Abstract: High reactivity coke is beneficial for achieving low carbon emission blast furnace ironmaking. Therefore, the preparation of highly reactive ferro-coke has aroused widespread attention. However, the effects of the particle size of iron ore on the pyrolysis behaviour of a coal-iron ore briquette are still unclear. In this study, the effect of three particle sizes (0.50–1.00 mm, 0.25–0.50 mm and <0.74 mm) of iron ore on the thermal and kinetic behaviours of coal-iron ore briquettes were investigated by non-isothermal kinetic analysis. The results showed that the synergistic effect of iron ore and coal during coking mainly occurred during the later reaction stage (850–1100 °C) and smaller particle sizes of iron ore have a stronger synergistic effect. The addition of iron ore had little effect on T_0 (the initial temperature) and T_p (the temperature at the maximum conversion rate) of briquette pyrolysis, however it greatly affected the conversion rate and T_f (the final temperature) of the briquettes. T_0 decreased with the decrease of iron ore particle sizes, while T_p and T_f showed opposite trends. After adding iron ore into the coal briquette, the reaction kinetics at all stages of the coal-iron ore briquettes changed. The weighted apparent activation energy of the caking coal (JM) briquette was 35.532 kJ/mol, which is lower than that of the coal-iron ore briquettes (38.703–55.627 kJ/mol). In addition, the weighted apparent activation energy gradually increased with decreasing iron ore particle sizes.

Keywords: coal-iron ore briquette; synergistic effect; iron ore; particle size; pyrolysis; kinetic

1. Introduction

Resource shortages and environmental problems are mutual challenges for the iron and steel industry all over the world. Promoting green growth is a common choice of the major economies in the world, and the efficiency of resources and energy utilization has also become an important factor to measure the competitiveness of the national manufacturing industry [1]. China is now the largest iron and steel producer and consumer in the world, accounting for nearly 50% of global steel output [2]. The iron and steel industry released 1.94 billion tons of CO₂, accounting for 16.7% of China's total CO₂ emissions [3]. At present, many ways of ironmaking are occupied in the world, and the blast furnace ironmaking accounts for almost 70% of the world's pig iron production [4]. In 2016, the total energy consumption of blast furnace ironmaking gained 1.11% compared to 2015 and reached 73.5% of the total energy consumption of the iron and steel enterprises in China [5]; blast furnace ironmaking is the main energy consumption and emission process in the iron and steel industry [6–8]. Therefore,

reducing blast furnace energy consumption has always been the focus of energy saving and emission reduction in the iron and steel industry [9].

To meet the demand for energy saving and emission reduction during the blast furnace ironmaking process, fundamental studies regarding the reactions in the blast furnace have emerged. Previous studies [10–12] have shown that for every 10 °C decrement in the thermal reserve zone (TRZ), the heat taken away by high-temperature gas decreased by approximately 23,036.8 kJ/ton of hot metal (tHM), and carbon combustion at the tuyere decreased by approximately 2.35 kg/tHM. Naito M [10] and H. Konishi et al. [13] have found that the use of highly reactive coke can reduce the temperature of the TRZ and increase the difference between the actual concentration and the equilibrium concentration of CO in the gas. These findings suggest that highly reactive coke not only decreased the fuel ratio, but also increased the driving force of the reduction reaction of the iron oxide, which is beneficial for an increase in the blast furnace output.

It was reported that the reactivity of coke can be increased by adding minerals with a catalytic effect [14,15]. At present, researchers generally believe that the minerals that can improve coke reactivity mainly include transition metals [16,17], alkali earth metals [18,19], and alkali metals [20–22]. However, alkali earth metal and alkali metal minerals have been studied quite thoroughly as catalysts, and these two kinds of minerals could destroy the lining of a blast furnace and aggravate the degradation of coke during the process of blast furnace production [23–26]. Therefore, ferro-coke was developed and iron, as the target product of blast furnace production, did not cause many adverse effects when iron ore was added to the coke [26]. Some authors, for examples Kasai et al. [9], Salahuddin et al. [27], and Murakami et al. [28], have confirmed that the reactivity of ferro-coke is obviously higher than that of traditional coke after adding iron minerals.

The addition of iron ore has a significant influence on the properties of ferro-coke, therefore it is necessary to consider the interaction behaviours of coal and iron ore during the coking process. Previous studies reported the influence of iron ore types on the pyrolysis of blended coal and coal-iron ore briquettes, however they did not take the effect of particle size into consideration [29,30]. Li Jinlian [31] reported the effect of the particle size of coal on the reduction and distributions of iron ore in the ferro-coke. However, the particle size of iron ore and the pyrolysis-reduction coupling kinetics of coal-iron ore briquettes were not taken into consideration. In previous studies [32–36], the blended coal as reductant was commonly less than 38% and the studies mainly focused on the percentage metallization of the iron ore and the strength of the briquettes. These kinds of studies can provide limited information for the manufacture optimization of ferro-coke. The properties of ferro-coke, such as gas generation, volume change, distributions of iron ore, and strength of ferro-coke, are mainly related to the pyrolysis behaviour of coal-iron ore briquettes. Hence, to determine an appropriate fabrication process of ferro-coke, the effect of the particle size of iron ore on the pyrolysis behaviour of caking coal during coking must be considered. These results can provide information regarding optimization of the manufacturing of ferro-coke.

The thermogravimetric (TG) and derivative thermogravimetric (DTG) analyses have been widely applied in kinetic behaviour analysis [37–40]. In this paper, the pyrolysis of coal or coal-iron ore briquettes were investigated experimentally using three particle sizes of iron ore by means of TG and DTG analyses. The effects of the different particle sizes of iron ore on the thermodynamic and kinetic behaviour of coal-iron ore briquettes, such as the rate-determining step and apparent activation energy, were revealed. The kinetic parameters of pyrolysis were calculated by a non-isothermal kinetic model. Additionally, the effects of different particle sizes on the mass loss were studied to evaluate the extent of the effect of iron ore on the coal-iron briquettes during coking.

2. Experimental

2.1. Raw Materials

One kind of caking coal (JM) and iron ore (EX) were selected from the BaoWuSteel Group Co., Ltd. (Wuhan branch, China). The proximate analysis of the caking coal was carried based on the Chinese standard GB/T212-2008. The ultimate analysis (content of C, H, O, N and S) in the caking coal was conducted based on the Chinese standards GB/T214-2007 and GB/T476-2008. These results are listed in Table 1. The chemical composition of coal ash was detected using an X-ray fluorescence method, and the results are shown in Table 2. The ash of the caking coal was made by air oxidation at 1088 K in a muffle furnace based on the Chinese standard GB/T 212-2008. The chemical composition and loss on ignition (LOI) of the iron ore sample was analysed and is presented in Table 3.

Table 1. Characterization data of the coal used in the experiments.

Sample	Proximate Analysis/Mass %, Air Dry Basis				Ultimate Analysis/Mass %, Ash Free Basis				
	Moisture	Volatiles	Ash	Fixed Carbon	C	H	N	S	O
JM	1.36	27.46	9.73	61.45	84.41	4.93	1.70	1.97	6.99

Table 2. Chemical composition of coal ash (mass %).

Sample	SiO ₂	Al ₂ O ₃	Fe ₂ O ₃	CaO	MgO	TiO ₂	SO ₃	K ₂ O	Na ₂ O
JM	52.62	33.43	8.26	1.97	0.38	0.28	1.46	0.28	0.26

Table 3. Chemical composition of the iron ores (mass %).

Samples	TFe	FeO	CaO	SiO ₂	MgO	Al ₂ O ₃	P	S	LOI
EX	55.15	0.82	0.19	11.59	0.34	4.55	0.13	0.02	1.63

2.2. Briquette Preparation

The coal and iron ore were both crushed using a laboratory roll crusher. Through sieving, the iron ore was separated into three size fractions (0.50–1.00 mm, 0.25–0.50 mm, and <0.074 mm), namely, EX1, EX2, and EX3, respectively. The coal powder particle sizes that were below 1 mm were used for further experiments, namely, JM. The full details of the coal-iron ore briquette preparation are given elsewhere [30] and only a summary is given here. Stoichiometrically, for 100 mg of briquettes, the wt % of the iron ore and coal was taken as 30% and 70%, respectively. A press machine was equipped to obtain the briquettes, which had a diameter of 6 mm and a height of 3 mm. The briquettes that contained EX1, EX2, and EX3 were named JE1, JE2, and JE3, respectively.

2.3. Pyrolysis Test

The pyrolysis experiments were performed in a thermal analyser (HCT-3, Henven Scientific Instrument Factory, Beijing, China), as shown in Figure 1. The apparatus mainly consisted of a vertical tube furnace which was equipped with an automatic balance with a detection precision of 1 µg. The balance, temperature, and gas flow controller were controlled by a computer. The experimental data can be collected and stored automatically by a customized software. About 100 mg of the prepared briquette was placed in an alumina crucible (φ8 mm × 1.5 mm) with a flow of 60 mL/min Ar. The research regarding the pyrolysis of the briquette was implemented by a non-isothermal method. The samples were heated at a heating rate of 20 °C from room temperature to 1100 °C. The mass loss and reaction rate of the samples can be represented as a function of temperature. According to the experimental data, the mass loss, conversion, and conversion rate can be expressed by the following equations:

$$\text{Mass loss} = \frac{m_0 - m_t}{m_0} \quad (1)$$

$$\text{Conversion } X = \frac{m_0 - m_t}{m_0 - m_f} \quad (2)$$

$$\text{Conversion rate} = -\frac{1}{m_0} \times \frac{dm}{dt} \quad (3)$$

where m_0 is the initial mass of the sample at time t_0 , mg; m_t is the mass of the sample at time t , mg; and m_f is the residual mass of the sample at the end of the reaction, mg.

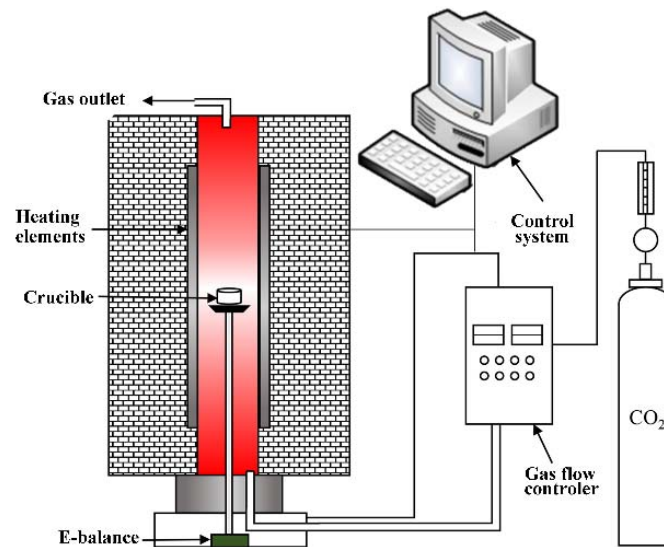


Figure 1. The scheme of the experimental facilities for pyrolysis.

2.4. X-ray Diffraction

The X-ray Diffraction (XRD) patterns were achieved by using a TTRIII type multipurpose X-ray diffractometer that was made in Japan. The samples in this study were crushed into a fine powder with particle sizes less than 0.074 mm. Then, the powders were packed into a holder. The copper $K\alpha$ radiation (30 kV, 30 mA, wavelength 0.1541 nm) was used as the X-ray source, and the scanned angular range varied from 10° to 90° with a scanning speed of $0.2^\circ/\text{s}$.

3. Results and Discussion

3.1. Characterization of the Raw Materials

In Tables 1 and 2, the coal that was used in this study has a relatively low ash content (9.73%) and a very low sulphur content (0.02%). The main composition of coal ash is SiO_2 (52.62%) and Al_2O_3 (33.43%). As shown in Table 3, the chemical composition of iron ore is dominated by Fe_2O_3 , SiO_2 , and Al_2O_3 . The iron ore has a small amount of MgO , CaO , and FeO . The XRD analysis of iron ores is shown in Figure 2, and the main minerals in EX are haematite (Fe_2O_3) and quartz (SiO_2). EX is oolitic haematite iron ore. Previous research [36,41] revealed that haematite together with gangue minerals, built the concentric shell of oolites and were intimately intergrown. The different particle sizes of EX iron ore may have a different effect on the pyrolysis reaction of the coal-iron ore briquettes and, thus, can affect the thermodynamic and kinetic behaviour of the briquettes.

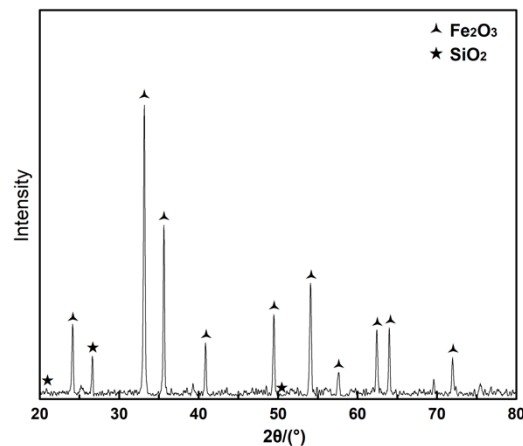


Figure 2. XRD analysis of iron ore.

3.2. Thermal Behaviour of an Iron Ore Briquette and a Coal Briquette

The mass loss curves of different sizes of EX show similar profiles (Figure 3a), indicating that the mass loss of these three particle sizes of iron ores changes slowly with increasing temperature due to moisture release and mineral decomposition. Additionally, larger particle size of EX exhibits a higher mass loss, which may be because the larger particles contain a higher moisture content. The maximum mass losses of EX1, EX2, and EX3 are 4.11%, 2.11%, and 2.50%, respectively.

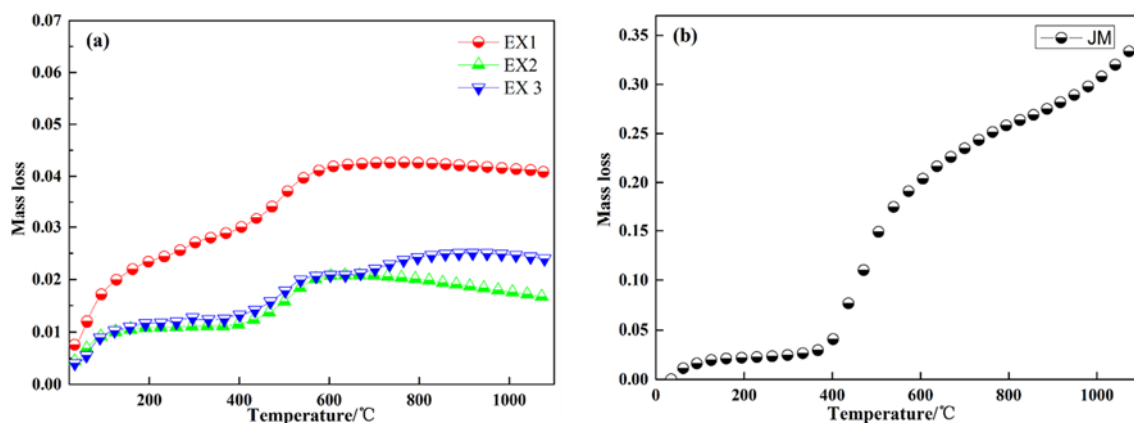


Figure 3. Mass loss for iron ore and coal (JM) under an Ar atmosphere: (a) the mass loss of different particle sizes of EX iron ore, (b) the mass loss of coal.

The pyrolysis curve of JM can be divided into three stages, which is similar to previous work [42]. From the mass loss curve of coal in Figure 3b, an initial mass loss of 2–3% is observed near 150 °C which is mainly because of the removal of the moisture content of the coal. Above 390 °C, the obvious mass loss indicates that the pyrolysis of coal has started. The period from 390 °C to 570 °C is the active decomposition stage of caking coal, which produces a large number of free radicals through depolymerization and decomposition reactions [43,44]. Therefore, a significant mass loss occurred. The gradual mass loss up to 1100 °C can be explained by the removal of the residual volatile matter in coal [45].

3.3. Effect on the Mass Loss of the Coal-Iron Ore Briquettes

To quantitatively analyse the effect of different particle sizes of iron ore in the coal-iron briquettes during coking, the theoretical mass loss of the briquettes was calculated based on the mean mass loss of iron ore and coal during separate pyrolysis processes. The calculated data was obtained as represented in the following equation:

$$x_{cal.} = 30\% \times x_{ore} + 70\% \times x_{coal} \quad (4)$$

where $x_{cal.}$, x_{ore} , and x_{coal} are the theoretical mass loss of the coal-iron ore briquettes, the mass of the iron ore briquettes, and the mass loss of the coal briquette, respectively, under an Ar atmosphere.

The interaction index α_T was applied to evaluate the effect of iron ore in the coal-iron briquettes during the coking process at different temperatures. The interaction index α_T was calculated from the following equation:

$$\alpha_T = \frac{x_{T(exp.)} - x_{T(cal.)}}{x_{T(cal.)}} \quad (5)$$

where $x_{T(exp.)}$ is the mass loss of coal-iron ore briquettes at temperature T and $x_{T(cal.)}$ is the theoretical mass loss of coal-iron ore briquettes at temperature T . The interaction indexes α_T are analysed as shown in Figure 4. A higher α_T value indicates a stronger synergistic effect of the iron ore and coal during coking. The interaction indexes α_T of JE1 and JE2 are almost the same before 850 °C and then increase quickly. Notably, α_T of JE3 decreases dramatically at approximately 400 °C and then increases with temperature. This behaviour may be caused by a strong depolymerization and decomposition reaction. In this period, large quantities of volatile matter (CO, CH₄ and CO₂) are generated and discharged. However, iron ore, which exists between coal particles, hinders the movement channel of the volatile matter and prolongs its discharge and then weakens the synergistic effect. All the α_T values of the coal-iron ore briquettes experience significant increases at around 850 °C due to the reduction of iron ore, according to Equations (6)–(11). Considerable H₂ gas is generated during the later stage of coking and promotes the reduction of iron ore. Therefore, the synergistic effect of iron ore and coal mainly occurs in the later reaction stage of coking and is much stronger than that in the primary stage. In addition, the promotion effect of the particle size of EX iron ore on the coal reaction during the later stage from high to low is 0.5–1.00 mm, 0.25–0.50 mm, and <0.074 mm, which indicates that the smaller particles of iron ore are more easily reduced during coking.

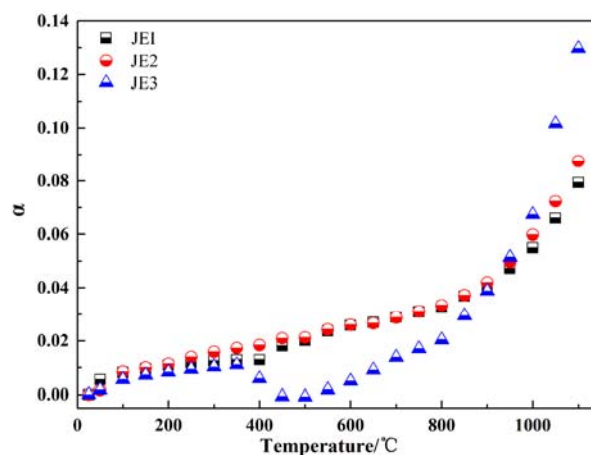


Figure 4. Experimental and calculated values of the coal-iron ore briquettes.

3.4. Effect on the Pyrolysis Characteristics of the Coal-Iron Ore Briquettes

The TG and DTG curves are shown in Figure 5 for the briquettes. Compared with JM, the conversion curves of JE1, JE2, and JE3 gradually move into the high-temperature region. From the DTG curves, the acute decomposition reaction region of coal is reduced due to iron ore addition. Furthermore, the reaction intervals of JE1, JE2, and JE3 sequentially decrease. In the range of 400–600 °C, the conversion rate of JM is higher than that of JE1, JE2, and JE3. However, the deviations between the coal briquette and coal-iron ore briquettes are closing with an increase in the temperature. The conversion rate of JE3 begins to exceed the other briquettes at the later reaction stage (approximately 800 °C) and shows a strong synergistic effect, which is consistent with the discussion in Section 3.3.

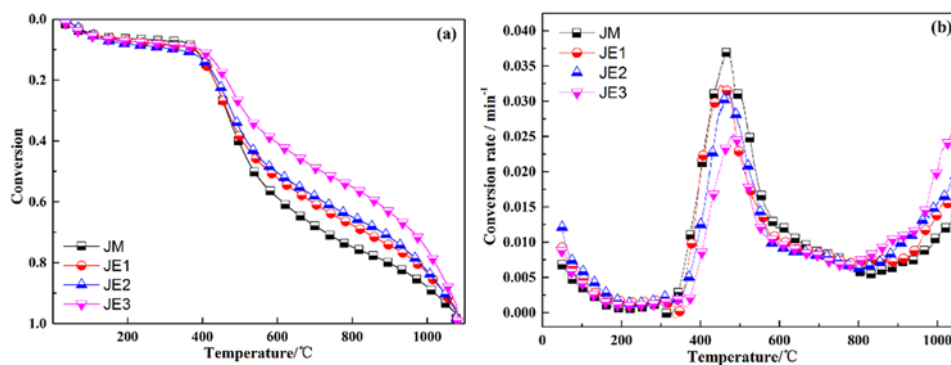


Figure 5. (a) Conversion and (b) conversion rate of the briquettes.

According to Figure 5, some characteristic temperatures [42] of pyrolysis can be analysed and are presented in Table 4. The start temperature of briquette pyrolysis T_0 is defined as the temperature at $x = 0.05$; T_p is temperature at the maximum conversion rate and the final temperature T_f is at $x = 0.85$. T_0 and T_f indicate the difficulty of the progress of the briquette pyrolysis reaction [46–48]. T_p is related to the coal structure. Normally, the coals that consist of the same structure have the same T_p . Table 4 shows that the different particle sizes of iron ore have little effect on the T_0 and T_p of the briquettes during coking. However, the addition of iron ore in the coal briquette results in T_f increasing by approximately 36–67 °C. The temperature region of intense pyrolysis directly determines the properties of coke, because the generation of metaplast will not be completed in an arrow temperature range [29,48]. From Figure 5, the acute decomposition reaction region of JM is broader than that of JE1, JE2, and JE3.

Table 4. The characteristic temperatures of different briquettes.

Samples	T_0 , °C	T_p , °C	T_f , °C
JM	104.51	466.12	976.68
JE1	109.36	451.25	1012.25
JE2	100.71	472.31	1015.03
JE3	91.49	486.03	1043.29

There is a significant increase in both the conversion and conversion rate at approximately 350 °C for all briquettes. This finding is because the mass loss before 350 °C is caused by the removal of adsorbed water, adsorbed gases, and carboxyl groups, which agrees with previous research [49]. Therefore, according to the analysis of TG and DTG curves, briquette pyrolysis can be divided into three reaction stages from 350 °C to 1100 °C [29].

3.5. Effect on the Kinetics of the Coal-Iron Ore Briquettes

The nomenclature report for symbols in the following equations can be seen in Table 5.

The mass loss rate of the briquettes during coking is a function of the reaction time and temperature and can be presented as:

$$\frac{dx}{dt} = k(T)f(x) \quad (12)$$

where $\frac{dx}{dt}$ is the weight loss rate, s^{-1} ; $k(T)$ is the rate constant, which is a function of temperature; $f(x)$ is the differential form of the reaction mechanism function; t is the reaction time, s ; and x is the reaction conversion.

Table 5. Nomenclature report for symbols.

Symbols	Description
$k(T)$	The rate constant
$f(x)$	The reaction mechanism function
A	The pre-exponential factor
E	The activation energy, kJ/mol
R	The standard molar gas constant, $\text{kJ mol}^{-1} \text{K}^{-1}$
β	The heating rate, $^{\circ}\text{C/min}$
E_n	The apparent activation during the different stages, kJ/mol
f_n	The percentage of the weight loss, %

The rate constant $k(T)$ is calculated by the Arrhenius equation:

$$k = A \exp\left(-\frac{E}{RT}\right) \quad (13)$$

where A is the pre-exponential factor; E is the activation energy, kJ/mol ; and R is the standard molar gas constant, $\text{kJ mol}^{-1} \text{K}^{-1}$.

During a non-isothermal process, the heating rate β is constant:

$$\beta = \frac{dT}{dt} \quad (14)$$

The following formula can be obtained from Equations (13) and (14):

$$\frac{dx}{dT} = \frac{A}{\beta} \exp\left(-\frac{E}{RT}\right) f(x) \quad (15)$$

Equation (15) can be integrated to give:

$$G(x) = \int_0^x \frac{dx}{f(x)} = \frac{A}{\beta} \int_0^T \exp\left(-\frac{E}{RT}\right) dT \quad (16)$$

Equations (17) and (18) can be obtained by the approximate calculation:

$$\frac{A}{\beta} \int_0^T \exp\left(-\frac{E}{RT}\right) dT \cong \frac{ART^2}{\beta E} \left(1 - \frac{2RT}{E}\right) \exp\left(-\frac{E}{RT}\right) \quad (17)$$

$$1 - \frac{2RT}{E} \cong 1 \quad (18)$$

The following formula can be obtained from Equations (17) and (18):

$$\ln\left[\frac{G(x)}{T^2}\right] = \ln\left(\frac{AR}{\beta E}\right) - \frac{E}{RT} \quad (19)$$

The expression $\ln(AR/\beta E)$ in Equation (19) is essentially constant. A straight line may be obtained if the left-hand side of Equation (19) is plotted versus $1/T$. From the slope, $-E/R$, the activation energy E can be determined. The intercept of the curve represents the value of pre-exponential factor A . The mechanism function can also be confirmed by the best fit between the theoretical curve and the

experimental curve. The mechanism functions that are commonly used in solid-phase reactions are listed in Table 6 [50–54].

Table 6. The common mechanism functions in pyrolysis reactions.

Mechanism	Code	Differential Form	Integral Form
Chemical reaction	N = 1	F1	$-\ln(1-x)$
	N = 2	F2	$(1-x)^{-1} - 1$
	N = 3	F3	$[(1-x)^{-1} - 1]/2$
Diffusion	The two-dimensional diffusion control	D2	$x + (1+x)\ln(1-x)$
	The two-dimensional diffusion control (Jander function)	D3	$[1 - (1-x)^{1/3}]^2$
	The three-dimensional diffusion control (Ginstling-Brounshten function)	D4	$(1 - 2x/3) - (1-x)^{2/3}$
Random nucleation and nuclei growth	Two dimensional	A2	$[-\ln(1-x)]^{1/2}$
	Three dimensional	A3	$[-\ln(1-x)]^{1/3}$

The weighted apparent activation energy [55] is used to evaluate the reactivity of the briquettes and can be expressed as Equation (20):

$$E_x = E_1f_1 + E_2f_2 + \dots + E_nf_n \quad (20)$$

where E_1 – E_n is the apparent activation during the different stages and f_1 – f_n is the percentage of the weight loss in the different stages. The weighted apparent activation of all the briquettes can be calculated using this method.

The fitting lines for the pyrolysis reaction of the JM briquette and kinetic parameters are shown in Figure 6 and Table 7, respectively. R^2 is the correlation coefficient. The larger the R^2 is, the better the correlation of the mechanism function is. The best fitting for both the first and second reaction stage is the F2 model, which indicates that the reaction is suitable for the chemical reaction ($n = 2$) model, whereas the best fitting for the third reaction stage is the D4 model. The model fitting results show that the early stage of the pyrolysis process is mainly controlled by a chemical reaction and the later stage is mainly controlled by diffusion. The activation energy of the first stage is the highest, mainly because of the decomposition of the polymer compound during 350–550 °C.

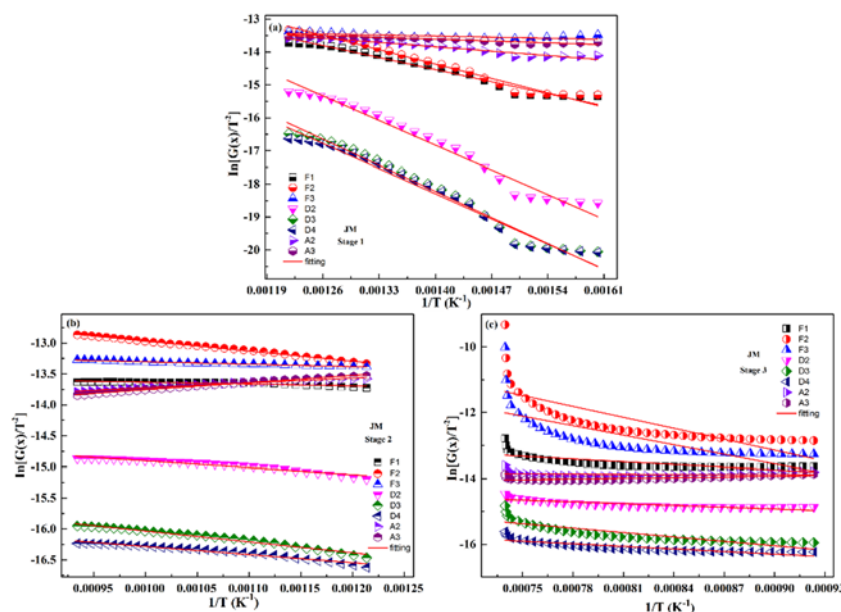


Figure 6. Linear fitting of the mechanism function during the different stages of the JM pyrolysis reaction: (a) linear fitting of the mechanism function at reaction stage 1, (b) linear fitting of the mechanism function at reaction stage 2, (c) linear fitting of the mechanism function at reaction stage 3.

Table 7. Kinetic parameters of the JM briquette using different mechanism functions.

Mechanism Functions	Stage 1 (350–550 °C)			Stage 2 (551–810 °C)			Stage 3 (811–1100 °C)		
	E/(kJ/mol)	A/s ⁻¹	R ²	E/(kJ/mol)	A/s ⁻¹	R ²	E/(kJ/mol)	A/s ⁻¹	R ²
F1	43.51	38.65	0.972	2.44	0.0047	0.799	22.85	0.35	0.535
F2	51.84	221.77	0.977	13.51	0.19	0.997	92.21	4691.9	0.553
F3	3.81	0.01	0.571	3.24	0.0096	0.977	80.31	744.25	0.497
D2	88.77	16,272.04	0.973	9.12	0.011	0.941	14.96	0.030	0.737
D3	93.78	9878.113	0.976	14.59	0.011	0.979	37.18	0.26	0.739
D4	93.43	5053.99	0.974	10.92	0.0041	0.959	21.82	0.023	0.749
A2	15.79	−0.26	0.947	−6.60	−0.003	0.983	1.31	0.0017	0.015
A3	6.56	0.03	0.872	−9.61	−0.003	0.994	−5.86	−0.003	0.427

The optimal mechanism function for all the coal-iron ore briquettes can be confirmed by the same analytical method above, as shown in Figure 7. The kinetic parameters are presented in Table 8. The three different kinds of coal-iron ore briquettes show the same reaction mechanism control according to the fitting results. The reaction mechanism control for all stages of JE1, JE2, and JE3 is diffusion control. The difference is that the diffusion control of the first and third stages are represented by the D2 model, whereas the second stage is fitted by the D3 model. Compared with the coal briquette, the reaction mechanism of coal-iron ore briquettes has obviously changed. The results indicate that after adding iron ore into the coal briquette, the iron ore particles will obstruct the gas diffusion and change the reaction mechanism from reaction control to diffusion control.

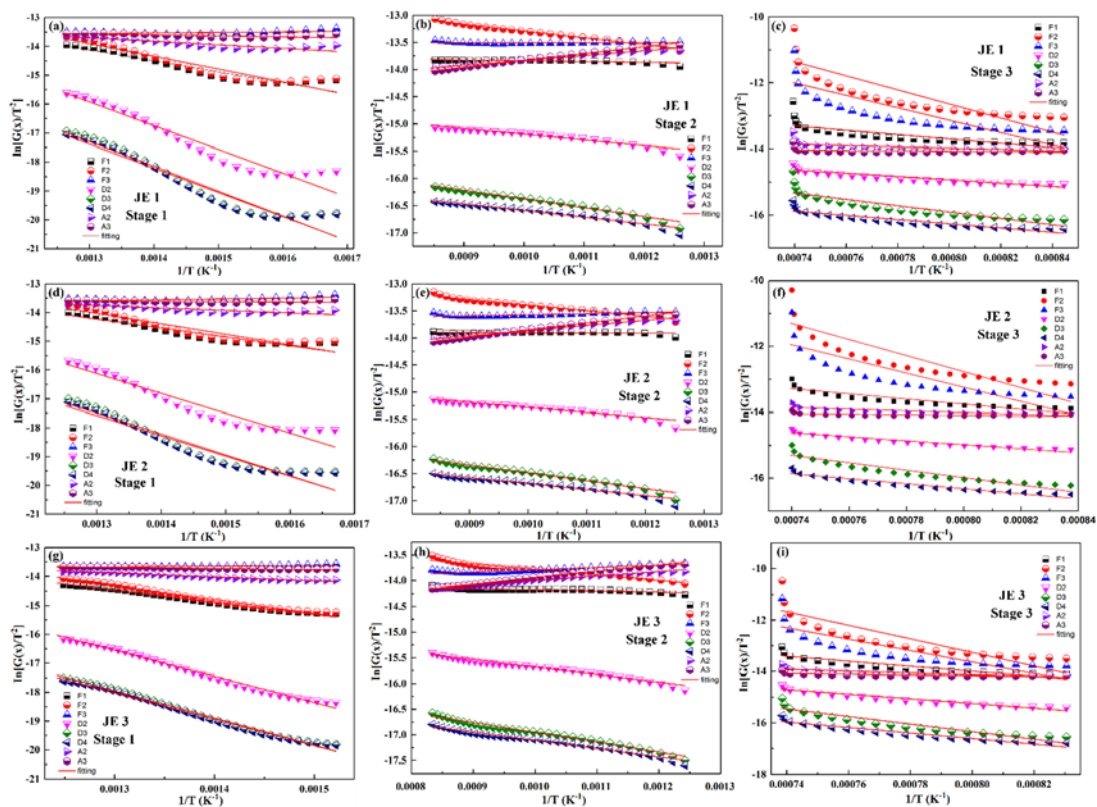


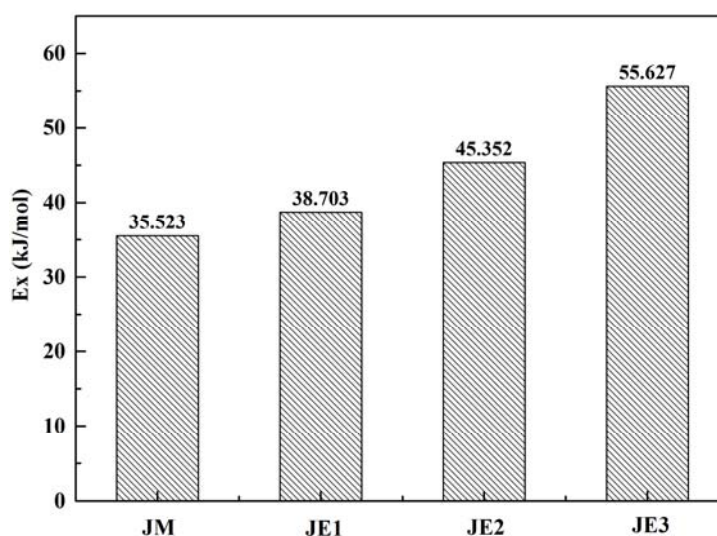
Figure 7. Linear fitting of the mechanism function at the different stages of the coal-iron ore briquette reaction: (a) linear fitting of JE1 at reaction stage 1, (b) linear fitting of JE1 at reaction stage 2, (c) linear fitting of JE1 at reaction stage 3, (d) linear fitting of JE2 at reaction stage 1, (e) linear fitting of JE2 at reaction stage 2, (f) linear fitting of JE2 at reaction stage 3, (g) linear fitting of JE3 at reaction stage 1, (h) linear fitting of JE3 at reaction stage 2, (i) linear fitting of JE3 at reaction stage 3.

Table 8. Kinetic parameters of the coal/coal-iron ore briquette at different reaction stages.

Samples	Stage/°C	Reaction Mechanism	E/(kJ/mol)	A/s ⁻¹	R ²
JE1	311–520	D2	57.20	52.58	0.939
	551–810	D3	13.43	0.0062	0.991
	811–1100	D2	40.97	0.828	0.874
JE2	326–525	D2	68.27	431.69	0.932
	526–920	D3	12.11	0.0043	0.978
	921–1100	D2	49.95	2.284	0.921
JE3	331–531	D2	75.04	729.01	0.992
	532–930	D3	15.98	0.0057	0.985
	931–1100	D2	75.26	30.20	0.925
JM	350–550	F2	51.84	221.76	0.977
	551–810	F2	13.52	0.193	0.997
	811–1100	D4	21.82	0.023	0.748

Comparing the activation energies of different samples, as shown in Table 8, at the first and third stages, all the activation energies for the coal-iron ore briquettes are larger than those of the coal briquette. These findings can be explained by two aspects. During the first reaction stage, the iron ore particles in the coal briquettes hinder gas diffusion, which results in an increase in the activation energies and a change in the reaction mechanism. During the third reaction stage, the increasing activation energies are due to the reaction of iron ore, which needs more energy. Furthermore, the activation energies during the first and third stages of JE1, JE2, and JE3 gradually increase. This increase implies that the smaller size of iron ore particles have a greater effect on the pyrolysis reaction of coal briquettes.

According to Equation (20), the weighed apparent activation energies of different briquettes can be obtained, as shown in Figure 8. The weighted activation energy of the coal-iron ore briquettes are approximately 38–55 kJ/mol, which are all larger than that of the JM briquette (35.523 kJ/mol). Previous studies [56,57] have shown that for the same coal, even though external factors (heating rate, gas atmosphere, etc.) change the activation energy at all stages of coal pyrolysis, the total activation energy required for pyrolysis remains constant. However, in this study, the addition of iron ore into the coal briquette not only changed the reaction activation energy of each stage, however it also changed the total activation energy. With a decrease in iron ore particles, the weighed apparent activation energy increases gradually.

**Figure 8.** Weighted apparent activation energies of the briquette samples.

3.6. Mechanism of the Synergistic Effect between Iron Ore and Coal during Coking

The whole pyrolysis reaction consists of several complex reactions, therefore, the synergistic effect between iron ore and coal was analysed particularly on two main stages, namely, the primary pyrolysis stage and secondary pyrolysis. The conceptual diagram of the synergistic effect between iron ore and coal during coking is illustrated in Figure 9. The iron ore particles are evenly distributed around the coal particles, as shown in Figure 9a. The decomposition and depolymerization reactions mainly occur during the primary stage of pyrolysis. A large number of volatile compounds including the reduction gases CO and H₂ are produced and discharged during this stage. The addition of iron ore particles reduces the thermal conductivity of the coal-iron ore briquette. A higher ambient temperature is required for pyrolysis to occur. Additionally, iron ore, which exists between coal particles, hinders the movement channel of the volatile matter and prolongs its discharge path. Therefore, the pyrolysis reaction is weakened by iron ore, and the smaller the iron ore particles are, the stronger the weakening effect is. The reduction of iron ore particles begins in the latter part of the primary pyrolysis stage. In Figure 9d, the reaction conforms to the unreacted core shrinkage model [37,58], which comes out along the surface of the iron ore particles during reduction. The reduction reaction occurs much more easily in smaller iron ore particles. The iron ore was completely reduced during secondary pyrolysis, which was proved by XRD analysis, as shown in Figure 10. The results show that even relatively large iron ore particle can be reduced completely during coking.

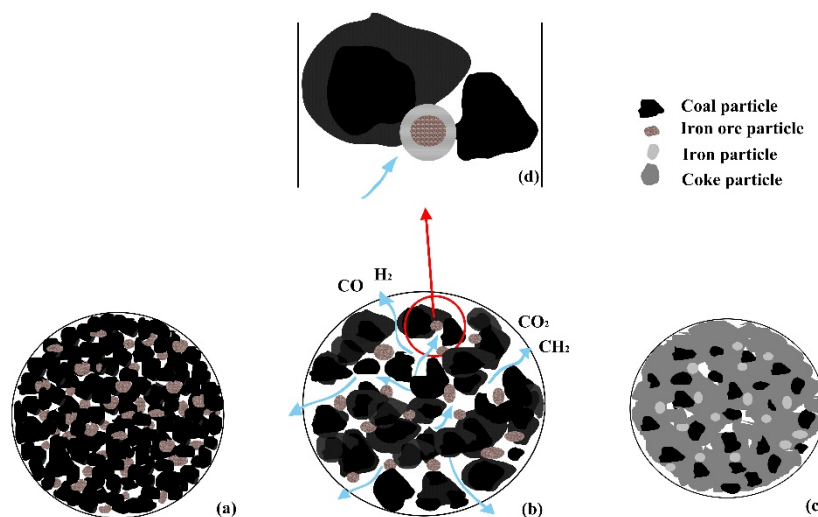


Figure 9. Conceptual diagram of the synergistic effect between iron ore and coal: (a) before pyrolysis; (b) the primary pyrolysis stage; (c) the secondary pyrolysis; (d) the reduction of iron ore particles.

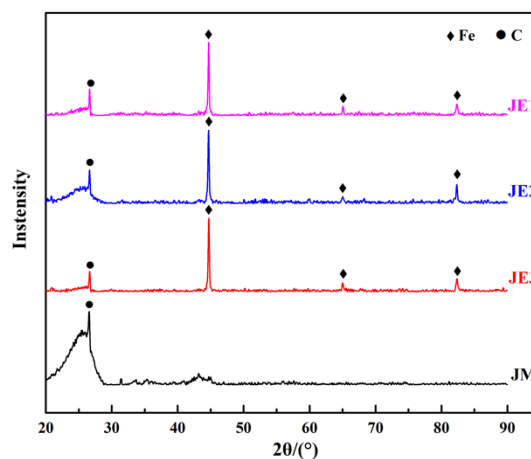


Figure 10. XRD patterns of the coal-iron ore briquette with different particle size iron ore after coking.

4. Conclusions

The iron ore (EX) that was used in this work is one of the natural iron ores that is difficult to be reduced in China because of the oolitic hematite structure. The main purpose of this paper was to describe the effects of the different particle sizes of the iron ore on the thermodynamic and kinetic behaviour of coal-iron ore briquettes during coking, and then to help make full use of the natural iron ore.

Being more specific, the pyrolysis of coal or coal-iron ore briquettes was investigated experimentally using three particle sizes of iron ore by means of TG and DTG analyses. The kinetic parameters of pyrolysis were calculated by a non-isothermal kinetic model. The effects of different particle sizes on the mass loss were studied to evaluate the extent of the effect of iron ore on the coal-iron briquettes during coking.

In all particle size ranges of iron ore, the interaction indexes α_T were positive, which means that the theoretical mass losses of the coal-iron ore briquettes are all lower than the experimental values. The synergistic effect of iron ore and coal mainly occurred during the later reaction stage of coking and was much stronger than that of the primary stage.

Then, compared with the coal briquette, decreasing the particle size of iron ore can increase T_f of the coal-iron ore briquette by 36–67 °C. The maximum reaction rates of briquettes occur at approximately 460 °C and decrease with a decrease in iron ore particle sizes in the following order: JM (0.0372 min⁻¹) > JE1(0.0324 min⁻¹) > JE2(0.0312 min⁻¹) > JE3(0.0253 min⁻¹). The results show that the particle sizes of iron ore can greatly affect the devolatilization rate of coal-iron ore briquettes.

Moreover, the kinetic analyses show that the first and second reaction stages for the pyrolysis reaction of the JM briquette are reaction controlled, and the third stage is mainly controlled by diffusion. The reaction kinetics at all stages of the coal-iron ore briquettes changed to a diffusion-controlled mechanism after adding iron ore into the coal briquette. The weighted apparent activation energy of the JM briquette was 35.532 kJ/mol, which was lower than that of the coal-iron ore briquettes. In addition, the weighted apparent activation energy increased gradually with a decrease in iron ore particles.

Finally, this study which was based on TG and DTG analyses demonstrated that the pyrolysis reaction of the coal-iron ore briquette is weakened by the iron ore particles, and the smaller the iron ore particles are, the stronger the weakening effect is. The reduction of iron ore particles begins during the latter part of the primary pyrolysis stage and is further enhanced during secondary pyrolysis. In addition, the relatively large iron ore particles can also be completely reduced during coking.

Author Contributions: H.Z., W.W., and R.X. conceived and designed the experiments; H.Z. and R.Z. performed the experiments; H.Z. and R.X. analysed the data and wrote the original manuscript; J.S. and Z.X. reviewed and corrected the paper.

Funding: This research was funded by the National Natural Science Foundation of China grant number 51704216, U1760101, 51474164, and Key Laboratory of Hubei Province for Coal Conversion and New Carbon Materials (Wuhan University of Science and Technology).

Acknowledgments: The authors acknowledge financial support from the National Natural Science Foundation of China (51704216, U1760101, 51474164) and Key Laboratory of Hubei Province for Coal Conversion and New Carbon Materials (Wuhan University of Science and Technology).

Conflicts of Interest: The authors declare no conflict of interest.

References

1. Gao, Y. Industrial green development 5-year plan issued. *Funct. Mater. Inf.* **2016**, *4*, 78. [[CrossRef](#)]
2. Xu, B.; Lin, B.Q. Assessing CO₂ emissions in China's iron and steel industry: A dynamic vector autoregression mode. *Appl. Energy* **2016**, *161*, 375–386. [[CrossRef](#)]
3. Xu, R.J.; Xu, L.; Xu, B. Assessing CO₂, emissions in China's iron and steel industry: Evidence from quantile regression approach. *J. Clean. Prod.* **2017**, *152*, 259–270. [[CrossRef](#)]

4. Sun, M.M.; Ning, X.J.; Zhang, J.L.; Li, K.J. Research status and progress of energy saving emission reduction technology for ironmaking. *China Met.* **2018**, *28*, 1–8. [[CrossRef](#)]
5. Planning Department of Ministry of Metallurgical Industry of China. *China Iron and Steel Statistics 2016*; Metallurgical Industry Publishing House: Beijing, China, 2016; ISBN 9787503765214. Available online: <https://www.amazon.cn/gp/product/B06X15HCNN?psc=1> (accessed on 24 August 2018).
6. Peng, J.Y.; Xie, R.; Lai, M.Y. Energy-related CO₂ emissions in the China's iron and steel industry: A global supply chain analysis. *Res. Conserv. Recycl.* **2018**, *129*, 392–401. [[CrossRef](#)]
7. Xu, B.; Lin, B.Q. Assessing CO₂ emissions in China's iron and steel industry: A nonparametric additive regression approach. *Renew. Sustain. Energy Rev.* **2017**, *72*, 325–337. [[CrossRef](#)]
8. Zhang, Q.; Li, Y.; Xu, J.; Jia, G.Y. Carbon element flow analysis and CO₂ emission reduction in iron and steel works. *J. Clean. Prod.* **2018**, *172*, 709–723. [[CrossRef](#)]
9. Li, K.J.; Zhang, J.L.; Zhang, Y.P.; Liu, Z.J.; Jiang, X. Analysis of the Development of ironmaking process based on the idea of Energy Saving and Emission reduction. *Process Eng. J.* **2014**, *14*, 162–172.
10. Naito, M.; Okamoto, A.; Yamaguchi, K.; Yamaguchi, T.; Inoue, Y. Improvement of Blast Furnace Reaction Efficiency by Temperature Control of Thermal Reserve Zone. Available online: <http://www.nssmc.com/en/tech/report/nsc/pdf/n9417.pdf> (accessed on 24 August 2018).
11. Kasai, A.; Matsui, Y. Lowering of Thermal Reserve Zone Temperature in Blast Furnace by Adjoining Carbonaceous Material and Iron Ore. *ISIJ Int.* **2004**, *44*, 2073–2078. [[CrossRef](#)]
12. Chen, L.B. *Blast Furnace Ironmaking Process and Calculation*; Metallurgical Industry Publishing House: Beijing, China, 1991; pp. 399–404. ISBN 7-5024-0849-5.
13. Konishi, H.; Ichikawa, K.; Usui, T. Effect of Residual Volatile Matter on Reduction of Iron Oxide in Semi-charcoal Composite Pellets. *ISIJ Int.* **2010**, *50*, 386–389. [[CrossRef](#)]
14. Shimoyama, I. Research Prospect on Coke Reactivity aiming at Low RAR Blast Furnace Operation. *Tetsu-to-Hagane* **2010**, *96*, 209–217. [[CrossRef](#)]
15. Du, H.J.; Yang, J.H. Catalytic effect of minerals on coke dissolution reaction in blast furnace. *Ironmaking* **2002**, *21*, 22–24. (In Chinese)
16. Wang, W.; Wang, J.; Xu, R.S.; Yu, Y.; Xue, Z.L. Influence mechanism of zinc on the solution loss reaction of coke used in blast furnace. *Fuel Process. Technol.* **2017**, *159*, 118–127. [[CrossRef](#)]
17. Ohtsuka, Y.; Kuroda, Y.; Tamai, Y.; Tomita, A. Chemical form of iron catalysts during the CO₂-gasification of carbon. *Fuel* **1986**, *65*, 1476–1478. [[CrossRef](#)]
18. Cazorla, D.; Linares, A.; Salinas, L.; Kyotani, T.; Yamashita, H.; Tomita, A. Carbon gasification catalyzed by calcium: A high vacuum temperature programmed desorption study. *Carbon* **1992**, *30*, 995–1000. [[CrossRef](#)]
19. Nomura, S.; Kitaguchi, H.; Yamaguchi, K.; Naito, M. The Characteristics of Catalyst-coated Highly Reactive Coke. *ISIJ Int.* **2009**, *47*, 245–253. [[CrossRef](#)]
20. Li, K.; Zhang, J.; Liu, Z.; Ning, X.; Wang, T. Gasification of Graphite and Coke in Carbon–Carbon Dioxide–Sodium or Potassium Carbonate Systems. *Ind. Eng. Chem. Res.* **2014**, *53*, 5737–5748. [[CrossRef](#)]
21. Dhube, A.P.; Gokarn, A.N.; Doraiswamy, L.K. Investigations into the compensation effect at catalytic gasification of active charcoal by carbon dioxide. *Fuel* **1991**, *70*, 839–844. [[CrossRef](#)]
22. Lei, Z.; Zhang, Y.; Cui, P. Investigate the kinetics of coke solution loss reaction with an alkali metal as a catalyst based on the improved genetic algorithm. *Int. J. Coal Sci. Technol.* **2017**, *2*, 1–9. [[CrossRef](#)]
23. Zhong, J.B.; Zhang, J.L.; Li, K.J.; Liu, Z.J.; Wang, C.; Zhao, D.; Zhang, H. The influence of simultaneous adsorption of potassium and sodium vapours on coke structure and performance. *Ironmak. Steelmak.* **2017**, *44*, 36–41. [[CrossRef](#)]
24. Li, K.J.; Zhang, J.L.; Barati, M.; Khanna, R.; Liu, Z.J.; Zhong, J.B.; Ning, X.J.; Ren, S.; Yang, T.J.; Sahajwalla, V. Influence of alkaline (Na, K) vapors on carbon and mineral behavior in blast furnace cokes. *Fuel* **2015**, *145*, 202–213. [[CrossRef](#)]
25. Li, K.J.; Zhang, J.L.; Liu, Z.J.; Wan, Q.; Ning, X.J.; Zhong, J.B.; Xu, R.S.; Wang, G.W.; Ren, S.; Yang, T.J. Zinc Accumulation and Behavior in Tuyere Coke. *Met. Mater. Trans. B* **2014**, *45*, 1581–1588. [[CrossRef](#)]
26. Higuchi, K.; Nomura, S.; Kunitomo, K.; Yokoyama, H.; Naito, M. Enhancement of Low-temperature Gasification and Reduction by Using Iron Coke in Laboratory Scale Tests. *ISIJ Int.* **2011**, *98*, 517–525. [[CrossRef](#)]

27. Salahuddin, N.; Elbarbary, A.; Allam, N.G.; Hashim, A.F. Reaction Behavior of Formed Iron Coke and Its Effect of Decreasing Thermal Reserve Zone Temperature in Blast Furnace. *Tetsu-to-Hagane* **2010**, *95*, 813–820. [[CrossRef](#)]
28. Murakami, T.; Kasai, E. Utilization of Ores with High Combined Water Content for Ore–carbon Composite and Iron Coke. *ISIJ Int.* **2011**, *51*, 1220–1226. [[CrossRef](#)]
29. Qiu, S.X.; Zhang, S.F.; Zhang, Q.Y.; Qiu, G.B.; Wang, L.Y. Effects of iron compounds on pyrolysis behavior of coals and metallurgical properties of resultant cokes. *J. Iron Steel Res.* **2017**, *24*, 1169–1176. [[CrossRef](#)]
30. Xu, R.S.; Dai, B.W.; Wang, W.; Johannes, S.; Xu, Z.L. Effect of iron ore type on the thermal behaviour and kinetics of coal-iron ore briquettes during coking. *Fuel Process. Technol.* **2018**, *173*, 11–20. [[CrossRef](#)]
31. Li, J.L.; Ren, W.; Tong, X.Y.; Wang, L. Study on reduction characteristics of iron oxide in ferrocoke. *Angang Technol.* **2016**, *5*, 13–16.
32. Sarkar, B.K.; Samanta, S.; Dey, R.; Das, G.C. A study on reduction kinetics of titaniferous magnetite ore using lean grade coal. *Int. J. Miner. Process.* **2016**, *152*, 36–45. [[CrossRef](#)]
33. Zhu, D.; Mendes, V.; Chun, T.J.; Pan, J.; Liu, Q.H. Direct Reduction Behaviors of Composite Binder Magnetite Pellets in Coal-based Grate-rotary Kiln Process. *ISIJ Int.* **2011**, *51*, 214–219. [[CrossRef](#)]
34. Tu, H.; Lv, X.W.; Bai, C.G.; Lun, Z.G.; Qiu, G. Reduction Behavior of Panzhihua Titanomagnetite Concentrates with Coal. *Metall. Mater. Trans. B* **2013**, *44*, 252–260. [[CrossRef](#)]
35. Man, Y.; Feng, J.X.; Li, F.J.; Ge, Q.; Chen, Y.M.; Zhou, J.Z. Influence of temperature and time on reduction behavior in iron ore–coal composite pellets. *Powder Technol.* **2014**, *256*, 361–366. [[CrossRef](#)]
36. Yu, W.; Sun, T.; Liu, Z.; Kou, J.; Xu, C. Effects of Particle Sizes of Iron Ore and Coal on the Strength and Reduction of High Phosphorus Oolitic Hematite-coal Composite Briquettes. *ISIJ Int.* **2014**, *54*, 56–62. [[CrossRef](#)]
37. Wang, G.; Zhang, J.; Hou, X.; Shao, J.; Geng, W. Study on CO₂ gasification properties and kinetics of biomass chars and anthracite char. *Bioresour. Technol.* **2015**, *177*, 66–73. [[CrossRef](#)] [[PubMed](#)]
38. Wang, G.W.; Zhang, J.L.; Shao, J.; Ren, S. Characterisation and model fitting kinetic analysis of coal/biomass co-combustion. *Thermochim. Acta* **2014**, *591*, 68–74. [[CrossRef](#)]
39. Wang, L.; Li, T.; Gabor, V.; Oyvind, S.; Terese, L. CO₂ Gasification of Chars Prepared by Fast and Slow Pyrolysis from Wood and Forest Residue: A Kinetic Study. *Energy Fuels* **2017**, *32*. [[CrossRef](#)]
40. Rousset, P.; Figueiredo, C.; Souza, M.; Quirino, W. Pressure effect on the quality of eucalyptus wood charcoal for the steel industry: A statistical analysis approach. *Fuel Process. Technol.* **2011**, *92*, 1890–1897. [[CrossRef](#)]
41. Yu, W.; Sun, T.C.; Kou, J.; Wei, Y.X.; Xu, C.Y.; Liu, Z.Z. The Function of Ca(OH)₂ and Na₂CO₃ as Additive on the Reduction of High-Phosphorus Oolitic Hematite-coal Mixed Pellets. *ISIJ Int.* **2013**, *53*, 427–433. [[CrossRef](#)]
42. Liu, Q.; Hu, H.Q.; Zhou, Q.; Zhu, S.W.; Chen, G.H. Effect of inorganic matter on reactivity and kinetics of coal pyrolysis. *Fuel* **2004**, *83*, 713–718. [[CrossRef](#)]
43. King, L.H.; Kelley, D.G. Investigation of the coking properties of coal by vacuum differential thermal analysis. *Econ. Geol.* **1955**, *50*, 832–854. [[CrossRef](#)]
44. Zhao, R.F.; Ye, S.F.; Xie, Y.S.; Chen, Y.F. Analysis of copyrolysis weight loss of coking coal, plastics and dust. *Environ. Sci.* **2003**, *24*, 28–33. (In Chinese)
45. He, X.M. *Coal Chemistry*; Metallurgical Industry Publishing House: Beijing, China, 2010; pp. 219–220. ISBN 9787502749797.
46. Zhang, X.D.; Zhao, Z.B. Study on the influence of Coalization degree and heating rate on Thermal decomposition. *Coal Convers.* **1999**, *2*, 43–47. (In Chinese)
47. Gao, J.S. *Coal Pyrolysis, Coking and Coal Tar Processing*; Chemical Industry Publishing House: Beijing, China, 2010; pp. 399–404. ISBN 9787122033840.
48. Liu, W. Study on the Effect of Iron-Bearing Minerals on Coal Pyrolysis Behavior and Coke Properties. Master's Thesis, Chongqing University, Chongqing, China, 2015.
49. Wang, J.H.; Chang, L.P.; Xie, K.C. Study on Pyrolysis characteristics and Kinetics of Western Coal. *Coal Convers.* **2009**, *32*, 1–5. (In Chinese)
50. Hu, R.Z.; Gao, S.L.; Zhao, Q.F. *Kinetics of Thermal Analysis*, 2nd ed.; Science Press: Beijing, China, 2008; pp. 219–220. ISBN 9787030202079.
51. Zuo, S.P.; Wu, Y.L.; Yang, M.D.; Zhang, J.L.; Li, C.; Tong, J.M. Characteristics and Dynamics of Pyrolysis Process Microalgae. *J. Combust. Sci. Technol.* **2007**, *13*, 330–334. (In Chinese)

52. Zhang, S.F.; Fu, Z.; Bai, C.G.; Wen, L.Y.; Peng, H.J. High temperature pyrolysis behaviour and kinetics of lump coal in COREX meltergasifier. *Ironmak. Steelmak.* **2013**, *41*, 219–228. [[CrossRef](#)]
53. Li, P.; Yu, Q.B.; Xie, H.Q.; Qin, Q.; Wang, Q. CO₂ Gasification Rate Analysis of Datong Coal Using Slag Granules as Heat Carrier for Heat Recovery from Blast Furnace Slag by Using a Chemical Reaction. *Energy Fuels* **2013**, *27*, 4810–4817. [[CrossRef](#)]
54. Vlaev, L.T.; Markovska, I.G.; Lyubchev, L.A. Non-isothermal kinetics of pyrolysis of rice husk. *Thermochim. Acta* **2003**, *406*, 1–7. [[CrossRef](#)]
55. Cumming, J.W. Reactivity assessment of coals via a weighted mean activation energy. *Fuel* **1984**, *63*, 1436–1440. [[CrossRef](#)]
56. Zhu, F. Pyrolysis Mechanism of Lump Coal and Combustion Behavior of Pulverized Coal Injection in COREX Melter Gasifier. Master's Thesis, Chongqing University, Chongqing, China, 2013.
57. Wang, Z.L. Study on the Characteristics of Minerals in Coal and Their Effects on the Structure and Properties of Coke. Master's Thesis, Anhui University of Technology, Ma'anshan, China, 2014.
58. Xu, R.S.; Dai, B.W.; Wang, W.; Johannes, S.; Bhattacharyya, A.; Xue, Z.L. Gasification Reactivity and Structure Evolution of Metallurgical Coke under H₂O/CO₂ Atmosphere. *Energy Fuels* **2018**, *32*, 1188–1195. [[CrossRef](#)]



© 2018 by the authors. Licensee MDPI, Basel, Switzerland. This article is an open access article distributed under the terms and conditions of the Creative Commons Attribution (CC BY) license (<http://creativecommons.org/licenses/by/4.0/>).